Available on the CERN CDS information server

CMS PAS TOP-21-007
TOTEM NOTE 2022-002

CMS Physics Analysis Summary

Contact: cms-pag-conveners-top@cern.ch

2022/03/13

Search for central exclusive production of top quark pairs in proton-proton collisions at $\sqrt{s} = 13\,\text{TeV}$ with tagged protons

The CMS and TOTEM Collaborations

Abstract

A search for the central exclusive production of top quark pairs ($t\bar{t}$) is performed using proton-tagged events in proton-proton collisions at the LHC at a centre-of-mass energy of 13 TeV. The data correspond to an integrated luminosity of $29.4\,\text{fb}^{-1}$. The $t\bar{t}$ decay products are reconstructed using the CMS central detector, while forward protons are detected with the CMS-TOTEM Precision Proton Spectrometer. An upper bound on the production cross section of 0.59 pb is set at 95% confidence level.

1 Introduction

Top quarks are copiously produced at the CERN LHC. At the LHC energies, the dominant production mode is via strong interaction processes, resulting in the production of top quark-antiquark pairs ($t\bar{t}$). The LHC experiments have measured the inclusive $t\bar{t}$ production cross section in proton-proton (pp) interactions at various centre-of-mass energies, using different top quark decay channels [1–10]. Top quarks can also be produced singly in electroweak processes in three different modes known as t channel, s channel, and tW associated production. The ATLAS and CMS Collaborations have observed or reported evidence for single top quark production in all three modes at different centre-of-mass energies [11, and references therein][12–14].

A different mechanism can lead to the production of top quark-antiquark pairs in pp scattering via the exchange of colourless particles such as photons or pomerons. In this case, one or both protons may remain intact after the interaction, while part of their energy is transferred to the $t\bar{t}$ pair. The process where the two protons survive the collision, i.e. the reaction $pp \to pt\bar{t}p$, is called central exclusive production. It receives contributions from quantum electrodynamics (QED) and quantum chromodynamics (QCD) diagrams, as sketched in Fig. 1.

Figure 1: Leading diagrams for $t\bar{t}$ central exclusive production, via $\gamma\gamma$ fusion (left) and pomeron exchange (right).

Predictions for central $t\bar{t}$ exclusive production in the framework of the standard model (SM) are available, including both QED and QCD contributions [15–20]. A critical element, in particular in the case of strong interaction processes, is the evaluation of the so-called rapidity gap survival probability, quantifying the probability of no additional soft interactions between the spectator partons of the colliding protons; these reinteractions may lead to additional final-state particles which fill the would-be rapidity gap and slow down or break up the outgoing protons, thus lowering the visible central exclusive production cross section. In general, predicted cross sections suffer from substantial uncertainties, but are usually in the $\mathcal{O}(0.1\,\text{fb})$ range for proton-proton collisions at $\sqrt{s} = 13\,\text{TeV}$. While the observation of the central exclusive production of $t\bar{t}$ pairs is only expected to become possible at the HL-LHC [21], contributions from physics beyond the SM could enhance the production cross section, making it detectable with the data collected so far.

This note reports on a search for central $t\bar{t}$ exclusive production at the LHC, carried out by reconstructing the top quarks from their decay products in the CMS central detector, and looking for the presence of two forward protons with the CMS-TOTEM Precision Proton Spectrometer (CT-PPS). At least one of the two W bosons from top quark decays is reconstructed in the $e\nu_e$ or $\mu\nu_\mu$ channel, while the other is reconstructed either in the leptonic or hadronic decay mode. The two scattered protons are reconstructed by CT-PPS, one on each side of the interaction region.

The note is organised as follows. Section 2 briefly illustrates the CT-PPS experimental setup and the reconstruction of basic objects; Section 3 specifies the data and simulation samples used in

the analysis; Section 4 outlines the analysis strategy, and details its various steps; Section 5 is devoted to the treatment of systematic uncertainties; finally, Section 6 describes the statistical analysis and presents the results; a summary is given in Section 7.

2 Tagged proton detectors and particle reconstruction

2.1 The CMS-TOTEM Precision Proton Spectrometer

CT-PPS [22] is an array of movable, near-beam devices, called Roman Pots (RP), enclosing tracking or timing detectors, and installed along the LHC beam line at about 210 m from the CMS interaction point (IP), on both sides, in LHC sectors 45 ("arm 0") and 56 ("arm 1"). A sketch of the system layout for one arm is shown in Fig. 2. During normal data taking, detectors are inserted horizontally, their edges approaching the beam as close as 2–3 mm from its nominal orbit, in order to reconstruct the flight path of protons coming from the IP. In this analysis, only the tracking stations are used. In 2017, when the data discussed here were collected, one station on each side was equipped with silicon strip detectors [23] and one with silicon 3D pixel detectors [24], at a distance of about 213 and 220 m from the IP, respectively. They can provide up to five and up to six measured points per track, respectively. Each strip tracker allows the reconstruction of at most one proton track per event: if hits compatible with more than one track are reconstructed, the event is discarded, to avoid ambiguities arising from wrong combinations of orthogonal strips. Each pixel tracker allows the reconstruction of multiple tracks per event, up to 10.

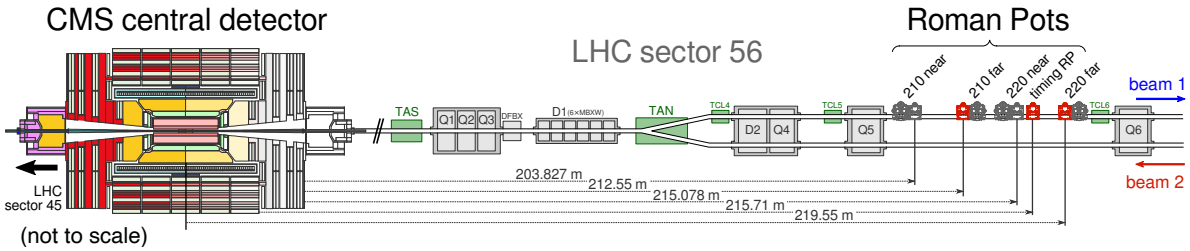

Figure 2: A schematic layout of one arm of CT-PPS along the LHC beam line. The RP shown in red are those used by CT-PPS; those in grey are part of the TOTEM experiment.

2.2 Particle reconstruction

In the central CMS detector, object reconstruction is based on the particle-flow (PF) algorithm [25], which aims at reconstructing and identifying each individual particle in an event, with an optimised combination of information from the various elements.

The electron momentum is estimated by combining the energy measurement in the ECAL, including all bremsstrahlung photons spatially compatible with originating from the electron track, with the momentum measurement in the tracker. The transverse momentum (p_T) resolution for electrons with $p_T \approx 45\,\text{GeV}$ from $Z \to ee$ decays ranges from 1.7% to 4.5% [26].

Muons are measured in the pseudorapidity range $|\eta| < 2.4$. Their energy is obtained from the curvature of the corresponding track; matching muons to tracks measured in the silicon tracker results in a relative transverse momentum resolution, for muons with p_T up to 100 GeV, of 1% in the barrel and 3% in the endcaps [27].

Jets are clustered from reconstructed particles using the anti-k_T algorithm [28, 29] with a distance parameter of 0.4. The jet momentum is determined as the vectorial sum of all particle

momenta in the jet, and is found from simulation to be, on average, within 5 to 10% of the true momentum over the whole p_T spectrum and detector acceptance. To mitigate effects from additional proton-proton interactions within the same or nearby bunch crossings ("pileup"), tracks identified to be originating from pileup vertices are discarded and an offset correction is applied to correct for remaining contributions. Jet energy corrections are derived from simulation studies so that the average measured energy of jets becomes identical to that of particle level jets. In situ measurements of the momentum balance in dijet, photon+jet, Z+jet, and multijet events are used to determine any residual differences between the jet energy scale in data and in simulation, and appropriate corrections are made [30]. The jet energy resolution amounts typically to 15–20% at 30 GeV, 10% at 100 GeV, and 5% at 1 TeV.

The missing transverse momentum vector $\vec{p}_T^{\,\text{miss}}$ is computed as the negative vector sum of the transverse momenta of all the PF candidates in an event, and its magnitude is denoted as p_T^{miss} [31]. The vector $\vec{p}_T^{\,\text{miss}}$ is modified to account for corrections to the energy scale of the reconstructed jets in the event.

The primary vertex (PV) is taken to be the vertex corresponding to the hardest scattering in the event, evaluated using tracking information alone, as described in Section 9.4.1 of Ref. [32].

Intact protons emerging from interaction vertices at small angles are reconstructed by the CT-PPS detectors, either from a single RP station (pixels or strips), or the combination of the information in two stations in the same arm (so-called multi-RP reconstruction). The latter features superior resolution, thanks to the lever arm between the two stations, while it suffers from lower efficiency because of the double track requirement. In this analysis, only multi-RP proton candidates are used. In this case, excluding the multi-track inefficiency of the strips mentioned in Section 2.1, which is treated separately, the proton reconstruction efficiency has two contributions: the efficiency of strip detectors, locally degrading in time because of radiation damage, and the multi-RP reconstruction efficiency, which combines the acceptance of protons propagating between the near and far station, the pixel detector efficiency (similarly affected by radiation damage), and the efficiency of the reconstruction algorithm. Efficiency values are provided as a function of the position of the track in the transverse plane, for each of two portions of the 2017 data-taking period. Scaling factors related to multi-track inefficiency are provided globally per arm, for each of six data-taking periods ("eras"). They represent the largest contribution to inefficiency, with values below 50% for the periods with the highest instantaneous luminosity.

The proton kinematics is characterised by the fractional momentum loss, defined as $\xi = (|\boldsymbol{p}_i| - |\boldsymbol{p}_f|)\,/\,|\boldsymbol{p}_i|$, where $\boldsymbol{p}_i$ and $\boldsymbol{p}_f$ are the initial and final proton momenta, respectively. The value of ξ is derived from the track parameters through detailed knowledge of the LHC magnetic lattice. Dedicated alignment and calibration procedures are in place for different fills and LHC optics setup [33]. The detector acceptance as a function of ξ is determined by the geometry of the detectors and the LHC collimators, and also depends on the specific LHC settings: in 2017 it was significantly different from zero in the region $0.02 < \xi < 0.2$.

3 Data and simulation samples

The analysis is based on data collected by CMS and CT-PPS in 2017. Only runs where all CT-PPS strip and pixel detectors were operational are considered: this results in a sample corresponding to an integrated luminosity of $29.4\,\text{fb}^{-1}$. The beam crossing angle at the IP, α_X, defined here as the angle between the LHC axis and one of the beams, was set at different values, with most data being recorded at $\alpha_X = 120$, 130, 140, or 150 μrad: the remaining data are

not included in this analysis.

To simulate the signal and background processes, different Monte Carlo (MC) event generators are used. For all processes, the response of the central CMS detector is simulated using the GEANT4 package [34], tuned on data.

A signal $pp \to p\gamma\gamma p \to pt\bar{t}p$ sample is produced using FPMC [35] as the matrix element generator, with the equivalent photon approximation (EPA) for the photon flux [36]. Events are generated for $0.02 < \xi < 0.2$. Top quark decays are simulated with MADSPIN [37], vetoing fully hadronic decays. The response of the CT-PPS detectors is simulated using a fast forward-proton simulation which includes beam-divergence and vertex smearing at the IP, along with their dependence on the beam crossing angle [33]. The outgoing protons are transported from the IP to the RPs. The aperture limitations for a given crossing angle are included in the simulation, and hits in the detectors are generated taking into account sensor acceptance and resolution. The simulated hits are then used to reconstruct proton tracks by means of the standard CT-PPS reconstruction algorithms.

The dominant background contribution is represented by inclusive $t\bar{t}$ production, with two uncorrelated protons from pileup interactions within the CT-PPS acceptance. Much smaller contributions come from single top quark production in the tW channel and, depending on the $t\bar{t}$ reconstruction mode, V + jets, VV, where V is either a W or a Z vector boson, and Drell–Yan (DY) events. The $t\bar{t}$ sample is simulated at next-to-leading-order (NLO) precision using the POWHEG (v2.0) [38–40] event generator. The inclusive $t\bar{t}$ production cross section is scaled to the best available theoretical prediction at next-to-next-to-leading order (NNLO) in QCD, amounting to 832 pb. For all background sources containing top quarks, the p_T spectra of top quarks in simulated samples are reweighted according to predictions at NNLO QCD accuracy [41]. For both signal and background event generation, a top quark mass of 172.5 GeV is assumed.

For all processes, the parton showering and hadronisation are simulated using PYTHIA 8 [42, 43] with the "CP5" underlying event tune [44]. The NNPDF3.1 [45] NNLO parton distribution functions (PDFs) are used as nominal choice.

4 Analysis flow

The analysis is conducted independently for the events with both W bosons decaying leptonically (dilepton mode) and for those in which one of them decays hadronically (ℓ + jets mode, where $\ell = e$ or μ); the results for the two modes are combined at the end.

4.1 Event selection

Events of interest are selected by CMS using a two-tiered trigger system. The first level (L1), composed of custom hardware processors, uses information from the calorimeters and muon detectors to select events at a rate of around 100 kHz [46]. The second level, known as the high-level trigger (HLT), consists of a farm of processors running a version of the full event reconstruction software optimised for fast processing, and reduces the event rate to around 1 kHz before data storage [47].

In the dilepton analysis, events must fire one of several trigger lines requiring the presence of either a single electron (isolated muon) with transverse momentum p_T greater than 35 (24) GeV, or two electrons (muons) with p_T greater than 23 and 12 (17 and 8) GeV, or an electron and a muon with p_T greater than 12 and 23 GeV or 23 and 8 GeV, respectively. Offline, both recon-

structed electrons and muons are required to pass a "tight" cut-based selection.

In the ℓ + jets analysis, events must fire a trigger requiring the presence of single electron (isolated muon) with p_T greater than 28 (27) GeV. Offline, reconstructed leptons must have $p_T > 30\,\text{GeV}$ and $|\eta| < 2.1$ (2.4) for electrons (muons).

For both decay channels, a weight is applied to simulated events as a function of the lepton p_T and η (and, for electrons, the data-taking period) to account for differences observed in the trigger efficiency between data and simulation.

Reconstructed jets are required to have $p_T > 30\,\text{GeV}$ (25 GeV) in the dilepton (ℓ + jets) channel, and $|\eta| < 2.4$. Moreover, lepton isolation cuts are applied, imposing that the angular distance $\Delta R = \sqrt{\Delta\eta^2 + \Delta\phi^2}$ between a jet and a lepton be at least 0.4.

Jets originating from the hadronisation of b quarks are identified with the DeepCSV algorithm [48] as b-tagged jets. The "medium" working point is used, corresponding to a typical efficiency of about 70% for correctly identified b quark jets, with a misidentification probability of 12 (1)% for c quark (light-flavour or gluon) jets.

The final selection in the dilepton mode requires the presence of at least two charged leptons; at least one of them is required to have $p_T > 30\,\text{GeV}$ and $|\eta| < 2.1$. The two leptons with the highest p_T are required to have opposite charge, and the dilepton system they form is required to have an invariant mass $M_{\ell\ell} > 20\,\text{GeV}$. For the events with two reconstructed leptons of the same flavour, the invariant mass of the dilepton system is required to be outside of the Z boson mass peak, within 15 GeV: $(M_{\ell\ell} < 76\,\text{GeV}) \cup (M_{\ell\ell} > 106\,\text{GeV})$. Events are categorised according to the final state leptons as electron-electron (ee), electron-muon ($e\mu$) or muon-muon ($\mu\mu$) events. Only events with at least two b-tagged jets are retained.

In the ℓ + jets analysis, the final selection requires the presence of exactly one lepton (electron or muon) satisfying the above requirements, at least 2 jets passing the b-tag selection and at least 2 jets failing the b-tag selection.

Both the dilepton and the ℓ + jets analysis require one multi-RP proton track to be reconstructed in each arm.

4.2 Top quark pair reconstruction

Full reconstruction of the top quark-antiquark pair allows the correlation of its kinematics with that of the forward protons. In central exclusive production, the invariant mass and the rapidity of the central system X is related to the momentum loss of the protons by the expressions

$$M_X = \sqrt{s\xi_1\xi_2}\,, \tag{1}$$

$$y_X = \frac{1}{2}\ln\frac{\xi_1}{\xi_2}\,, \tag{2}$$

where $\sqrt{s}$ is the centre-of-mass energy and ξ_1, ξ_2 are the fractional momentum losses of the outgoing protons in the positive and negative z direction, respectively. The reconstruction of top quark-antiquark candidates through their decay chains is carried out independently for the dilepton and ℓ+jets modes; the kinematics matching with the tagging protons is exploited differently: in the first case it enters implicitly the multivariate discriminant described in Section 4.4, while in the second case it is explicitly used as a constraint in a global kinematic fit.

In the dilepton analysis, the two leptons and the two b-tagged jets with the highest p_T are selected. The association of the leptons to the jets relies on a kinematic reconstruction algorithm [49] that also estimates the kinematics of the top quark and antiquark. The missing transverse momentum is assumed to originate solely from the two neutrinos in the decay, and the W boson and top quark masses, m_W and m_t, are constrained to their known values. Multiple replicas of the energy-momentum conservation equations are generated, with particle momenta varied according to their resolution and the width of the W boson; for each of them, the solution with the smallest value of the $t\bar{t}$ invariant mass is chosen, and a weight is assigned based on the spectrum of the true invariant mass of the lepton and b jet system. The weights are then used to obtain weighted averages of the kinematic observables of the top quark and antiquark, and their sum over the replicas is used to choose the best combination of leptons and jets. This algorithm finds a physical solution in about 90% of the events passing the previous selection. The remaining events are kept and their $t\bar{t}$ variables assigned a conventional negative value, so that they can contribute to the training of the classifier described in Section 4.4.

In the ℓ+jets analysis, the highest p_T b-tagged jets and light-flavour jets are considered; up to four of each type are selected. Top quark candidates with the W boson decaying leptonically are reconstructed from combinations of a b-tagged jet, the selected lepton and a neutrino candidate. The neutrino candidate is initially reconstructed from the missing transverse momentum, with the longitudinal component of momentum assigned by imposing the constraint $M_{\ell\nu} = m_W$. In case the two solutions of the resulting quadratic equation are real, that closer to the p_z value of the lepton is chosen. Top quark candidates with the W boson decaying hadronically are reconstructed from combinations of a b-tagged and two light-flavour jets. The choice of the two b jets to be used for top quark reconstruction, and of their association with the other objects, is based on the invariant mass of the reconstructed top quark and antiquark candidates, $m_t^{(reco)}$ and $m_{\bar{t}}^{(reco)}$. The combination that yields the lowest value of $|m_t^{(reco)} - m_t^{(ref)}| + |m_{\bar{t}}^{(reco)} - m_t^{(ref)}|$, where $m_t^{(ref)} = 173.1\,\text{GeV}$, is selected. Using this procedure, b jets are found to be correctly assigned in 75% of all cases. The kinematic observables of all reconstructed objects are further corrected by means of a kinematic fit. The momentum components of the lepton, of all jets and of the neutrino, as well as the fractional momentum loss of the forward protons are allowed to float in the fit, with Gaussian probability distribution functions centred on their measured values and with width equal to the measurement uncertainty; the longitudinal component of the neutrino momentum is left free to float in the fit. The invariant masses of the top quark and W boson candidates are constrained to their known values; the total transverse momentum of the $t\bar{t}$ system is set to zero; finally, the invariant mass of the $t\bar{t}$ system and the fractional momentum loss of the protons are required to satisfy Eq. (1), where X is the $t\bar{t}$ pair. The fit is found to improve the resolution on the $M_{t\bar{t}}$ measurement by about a factor 2.

Figure 3 shows the resolution achieved on the invariant mass of the $t\bar{t}$ pair for the two reconstruction modes.

4.3 Signal and background models

The presence of multiple proton interactions within the same LHC bunch crossing results in the superposition of objects from different primary vertices both in the central CMS apparatus and in CT-PPS. The probability to have at least one proton in the acceptance of a given arm of CT-PPS, for any bunch crossing, ranges between about 40% and 70% depending on the LHC optics settings and instantaneous luminosity. However, while the pileup activity in the central detector can be modelled with adequate accuracy, no simulation has been validated so far to include additional protons from uncorrelated diffractive events, where the proton scattering

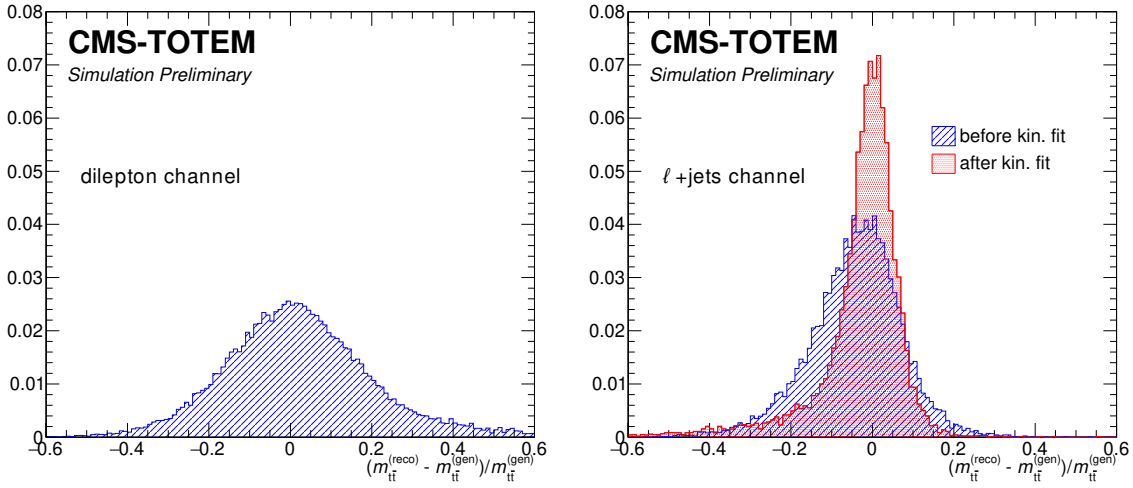

Figure 3: Normalised distribution of the relative invariant mass resolution of the reconstructed $t\bar{t}$ system for the dilepton (left) and ℓ+jets (right) analyses. For the ℓ+jets mode, the hatched blue and dotted red histograms represent the distribution before and after applying the kinematic fit, respectively.

is mediated by strongly interacting colour-singlet exchange: as a consequence, in MC samples, background events contain no forward protons, while signal events contain exactly two forward protons on opposite sides (though not necessarily within acceptance).

The presence of pileup protons, uncorrelated with the event reconstructed in the central detector, has two effects:

- a background event may be selected because exactly one random proton per arm has been reconstructed in CT-PPS;
- a signal event may be rejected because of the multi-proton reconstruction inefficiency, or it may be wrongly reconstructed because a background proton is selected instead of the signal one that went undetected as a result of detector inefficiency or limited acceptance.

In order to take this correctly into account, a pool of proton pairs reconstructed in real data is collected to be used as pileup protons, from events subject to the same requirements as signal events except for those on the presence of tagged protons and on the number of b-tagged jets. Moreover, the proton reconstruction efficiency as a function of ξ and the probability of having 0 (not including multi-track inefficiency) or 1 proton reconstructed in each arm are taken from dedicated studies on data [33]. Because the detector and beam conditions varied significantly throughout the data taking, both the proton pools and the efficiency/probability values are considered separately for each of the five eras (B, C, D, E, abd F) and, except for the reconstruction efficiency, for four values of the beam crossing angle α_X at the IP (120, 130, 140, 150 μrad).

For each simulated event, a pair of protons is selected from the pool according to the relative normalisation of the (era, α_X) samples. Then the following procedure is applied:

- for background events, the proton pair is added and a weight corresponding to the probability of reconstructing one proton in both arms is assigned;
- for signal events, first the number of reconstructed simulated protons is determined according to the detector acceptance and a random correction based on the recon-

struction efficiency; if only one of the original protons is left, the other is replaced with one from the pool, and an appropriate weight is assigned to the event, according to the probability for ending up with exactly one proton per arm; events where both simulated protons are not reconstructed are treated as background.

In order to match the pileup conditions for simulated events to those in real data, a further reweighting procedure is applied to simulated events, based on the number of reconstructed interaction vertices. The distribution of this number for a given simulated sample, $P^{\mathrm{MC}}(n_{\mathrm{vtx}})$, and that for the data in each of the 20 (era, α_{X}) regions, $P^{\mathrm{data}}(n_{\mathrm{vtx}} \mid \mathrm{era}, \alpha_{\mathrm{X}})$, are determined. A further weight $w_{\mathrm{PU}} = P^{\mathrm{data}}(n_{\mathrm{vtx}} \mid \mathrm{era}, \alpha_{\mathrm{X}}) / P^{\mathrm{MC}}(n_{\mathrm{vtx}})$ is assigned depending on the sampled region.

To assess the validity of the background model obtained from this procedure, the distributions of various event variables in data and simulated samples are compared; very good agreement is observed. Figure 4 shows the overall distribution of the proton fractional momentum loss ξ in both arms of CT-PPS for the semileptonic mode.

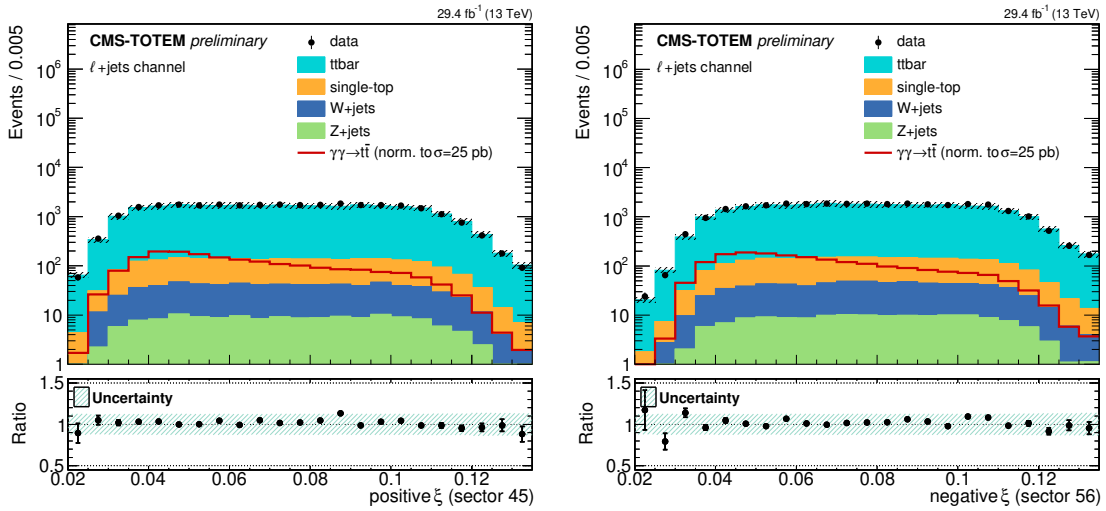

Figure 4: Distribution of the proton fractional momentum loss ξ in data and background simulated samples after pileup proton mixing and pileup reweighting, in the ℓ + jets channel. Solid histograms: background; open histogram: signal, normalised to a cross section of 25 pb, approximately 10^5 larger than the SM cross section prediction from [18]; points with error bars: data.

4.4 Multivariate analysis

In order to enhance the signal content of the selected samples, information from variables showing discriminating power against background sources is efficiently exploited by means of multivariate analysis techniques. For both the dilepton and the ℓ+jets channels, a boosted decision tree (BDT) algorithm [50] is used, implemented in the TMVA toolkit [51]. The samples used for the training consist of signal events with both protons reconstructed, and inclusive $\mathrm{t\bar{t}}$ production events, by far the largest source of background, with two pileup protons added from real data as described in the previous section. Because of the different objects in the final state and their related kinematics, the choice of the discriminating variables is independent for the two modes.

For the dilepton mode, the following 15 kinematic variables are used: the mass and the rapidity of the central system reconstructed both from the $\mathrm{t\bar{t}}$ decay products and from proton kinematics

(Eqs. (1), (2)); $p_{\mathrm{T}}^{\mathrm{miss}}$; the invariant mass and the angular distance ΔR of the two leptons; $|\Delta\phi|$ of the two selected b-tagged jets; the rapidity of the system formed by the two b-jets and the two leptons, and the sum of the absolute values of their individual rapidities; the rapidity of the system formed by all other reconstructed jets, and the sum of the absolute values of their individual rapidities; the squared energy sum for all objects used for the $\mathrm{t\bar{t}}$ reconstruction; the minimum absolute value of the rapidity difference for any two systems formed by a lepton and a b-tagged jet; the number of light-flavour jets.

For the ℓ+jets mode, the following 10 kinematic variables are used: the number of light-flavour jets and of b-tagged jets; the sum of the invariant mass of all jets; the total energy of all light-flavour jets; the mean ΔR for all pairs of light-flavour jets; the total energy of all extra jets (not used for $\mathrm{t\bar{t}}$ reconstruction); the lepton momentum and its isolation; the difference in central system rapidity reconstructed from the $\mathrm{t\bar{t}}$ and the pp systems (Eq. (2)); the χ^2 of the kinematic fit.

The distributions, for signal and background, of some of the kinematic variables of interest are shown in Fig. 5 for the two modes.

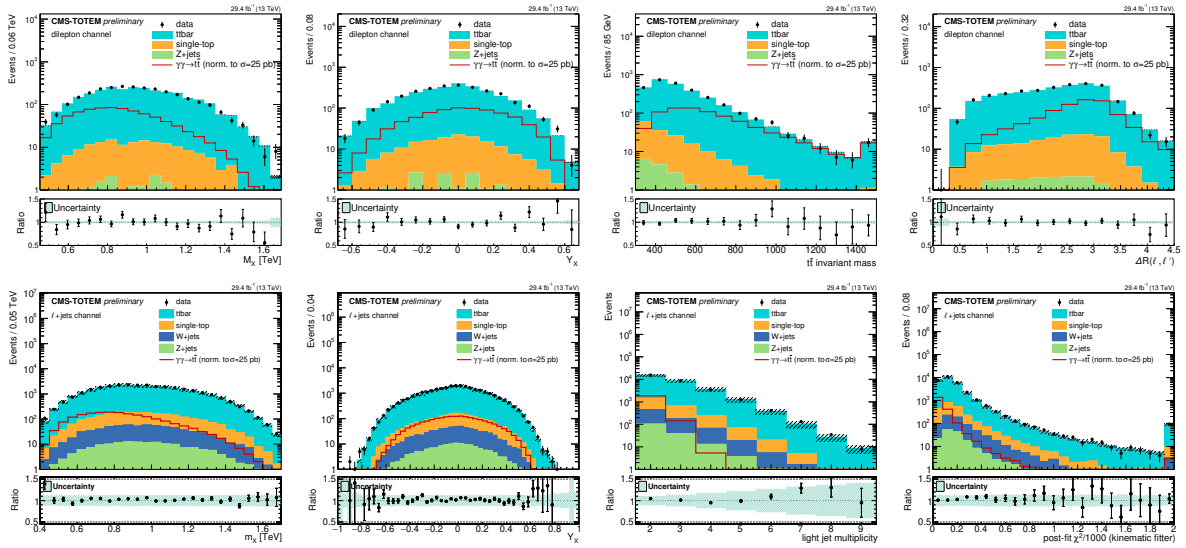

Figure 5: Distribution of some of the kinematic variables of interest for the dilepton (top) and ℓ+jets (bottom) analysis. Solid histograms: background; open histogram: signal, normalized to a cross section of 25 pb, approximately 10^5 larger than the SM cross section prediction from [18]; points with error bars: data.

5 Systematic uncertainties

Several sources of systematic uncertainty affect the normalisation of the signal and background yields, as well as the shape of the BDT output used as the final discriminant. For each of them, the impact on the final result is assessed by varying appropriately the parameters involved, and repeating the analysis. When the variations imply a change in the BDT shape, a smoothing procedure (using the '353QH' algorithm described in [52]) is applied to the associated template used in the fitting procedure described in Section 6. Modified BDT shapes are compared to the nominal one using the Kolmogorov–Smirnov test: if the significance of the test is above 95% for both the upwards and downwards variation, the corresponding systematic uncertainty is only further considered as an overall normalisation effect.

The sources of systematic uncertainties can be subdivided into experimental and theoretical components.

Experimental uncertainties The measured integrated luminosity that is used to normalise the MC predictions has an associated systematic uncertainty of 2.3% [53]. Several uncertainties arise from the reconstruction and identification of various objects. For leptons, b jets, and forward protons, efficiency correction scale factors are varied within their uncertainties, which affect both the shape and normalisation of the final discriminant. The uncertainty in the jet energy has an effect on the reconstruction of the kinematic variables used to calculate the discriminants: the corresponding uncertainty is evaluated by rescaling the p_{T}- and η-dependent scale factors of the reconstructed jet energy [30] and jet energy resolution. The variation in four-momentum for each selected jet is propagated to $\vec{p}_{\mathrm{T}}^{\,\mathrm{miss}}$ and the b tagging scale factors. Uncertainties in the efficiency corrections for the lepton trigger are estimated as a function of the lepton p_{T} and η from control samples in data; for muons (electrons) they are well below 1% (within 3%), except for $p_{\mathrm{T}} < 35\,\mathrm{GeV}$, where they range up to 3% (8%). In the pileup proton enrichment procedure described in Section 4.3, the normalisation of the simulated data samples is performed according to the pileup proton rate measured in real data with no requirement on b jet multiplicity. A possible bias of the proton tag rate arising from the different b jet selection is estimated by measuring the proton tag rate again after requiring $N_{\mathrm{b\,jet}} \geq 1$: the difference in the predicted tagged proton rate is taken as the corresponding systematic uncertainty. For the signal sample, the simulation of forward protons is tuned to reproduce the expected bias and resolution in ξ reconstruction assuming perfect knowledge of the detector alignment and LHC optics. The effect of uncertainties in this assumption is estimated by shifting, in each event, the reconstructed ξ values according to the "systematics" contribution described in [33].

Theory uncertainties The uncertainties related to the choice of the QCD factorisation and renormalisation scales at the matrix-element level are estimated by varying them independently by factors 2 and 0.5. For PDF modeling, two effects are considered: a variation of α_{S}, and the RMS of the variations from a collection of PDF error eigenvectors sets, as described in the PDF4LHC recommendations guide [54]. The uncertainty associated to parton shower emission in initial and final state (ISR and FSR) is evaluated by varying the strong coupling constant by a factor 2 and 0.5. The normalisation of the inclusive $\mathrm{t\bar{t}}$ background is set free to vary around its nominal values for the ℓ + jets and the dilepton channels separately, while single top quark and electroweak background normalisation uncertainties are taken to be 5% and 30%, respectively. Finally, the effect of the finite size of the simulated samples used for the analysis is taken into account with the Beeston–Barlow method [55]. While no uncertainty is attributed to the choice of the event generator for the inclusive $\mathrm{t\bar{t}}$ background, it has been verified that when using aMC@NLO as an alternative generator, the change in the expected and observed limits is well within one standard deviation (σ).

6 Results

Upper limits on the cross section for the two decay modes considered are obtained from binned fits to the distributions of the BDT variables: the extraction of the limits is based on an asymptotic approximation of the distributions of the test statistics, which in turn is based on the profile likelihood ratio, under given hypotheses for the signal and the background [56]. All sources of systematic uncertainty are included in the fit as nuisance parameters, except those whose impact is lower than 0.1%.

In the dilepton analysis, the fit is performed simultaneously for each of the final state lepton

combinations ee, eμ, $\mu\mu$. In the ℓ+ jets analysis, the fit is performed simultaneously on each of the 20 samples defined by (era, α_X).

The expected and observed distributions of the BDT variable for the dilepton and ℓ+jets decay modes are shown in Fig. 6, where all signal regions are combined.

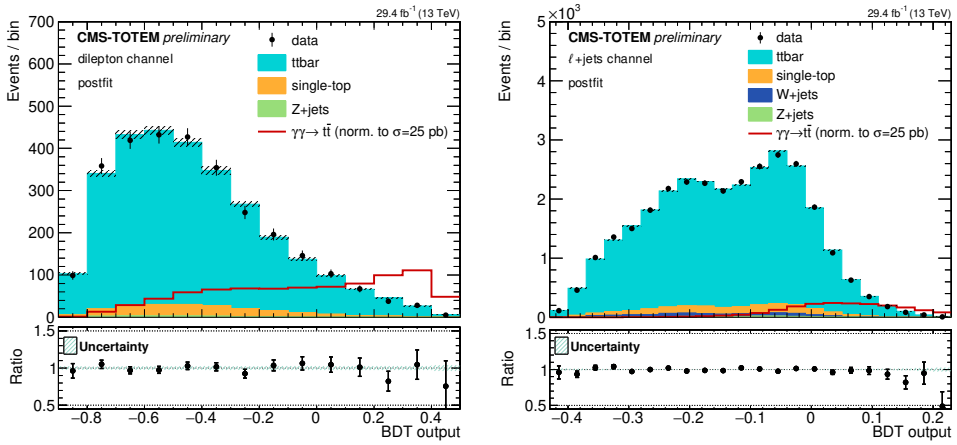

Figure 6: Distribution of the BDT score in the signal region for simulated events after the fit, and for data. Left: dilepton mode; right: ℓ+jets mode. The red open histogram shows the expected distribution for signal, normalized to a cross section of 25 pb, approximately 10^5 larger than the SM cross section prediction from [18];. For both reconstruction modes, all signal regions are combined.

In the dilepton mode, the fit returns an observed (expected) 95% confidence level (CL) upper limit of 1.70 pb (2.02 pb); in the ℓ+jets mode an observed (expected) limit of 0.78 pb (1.54 pb) is obtained.

The two modes are then considered jointly in a combined fit, where all sources of systematic uncertainty are treated as fully correlated between the two analyses. The observed (expected) limit resulting from the combined fit is 0.59 pb (1.14 pb).

The results of the fit are shown in Fig. 7, for the individual reconstruction modes as well as for the combination. The value of the extracted limit depends mostly on the statistical precision; the effect of systematic uncertainties is about 10%, the most important contributions being those related to background normalisation, FSR modelling, jet energy corrections and resolution, and proton reconstruction with PPS.

7 Summary

In summary, we have searched for the central exclusive production of top quark-antiquark pairs in proton-proton interactions, $pp \to pt\bar{t}p$, for the first time using tagged intact protons, reconstructed by the CMS-TOTEM Precision Proton Spectrometer. The $t\bar{t}$ pairs are reconstructed by the CMS detector either in the dilepton or the lepton+jets decay modes: the search is conducted separately for the two modes, and the results are combined at the end. With a data sample of proton-proton collisions at a centre-of-mass energy of 13 TeV, corresponding to an integrated luminosity of 29.4 fb^{-1}, results consistent with predictions from the standard model are obtained, and an upper limit of 0.59 pb at the 95% confidence level is set on the central exclusive production of $t\bar{t}$ pairs.

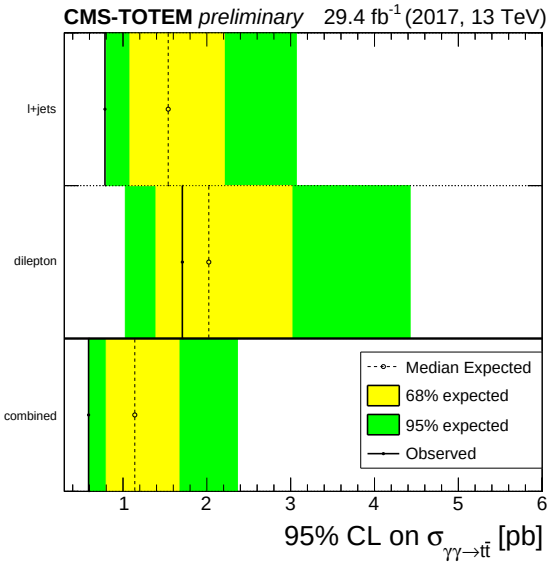

Figure 7: Expected 95% CL upper limit for the signal cross section, for the two reconstruction modes and for the combination. The green and yellow bands show the $\pm 1\sigma$ and $\pm 2\sigma$ intervals, respectively.

References

[1] CMS Collaboration, "Measurement of the inclusive $\mathrm{t\bar{t}}$ cross section in pp collisions at $\sqrt{s} = 5.02$ TeV using final states with at least one charged lepton", *JHEP* **03** (2018) 115, doi:10.1007/JHEP03(2018)115, arXiv:1711.03143.

[2] ATLAS Collaboration, "Measurement of the top quark pair production cross-section with ATLAS in the single lepton channel", *Phys. Lett. B* **711** (2012) 244, doi:10.1016/j.physletb.2012.03.083, arXiv:1201.1889.

[3] ATLAS Collaboration, "Measurement of the $t\bar{t}$ production cross-section using $e\mu$ events with b-tagged jets in pp collisions at $\sqrt{s}$ = 7 and 8 TeV with the ATLAS detector", *Eur. Phys. J. C* **74** (2014) 3109, doi:10.1140/epjc/s10052-016-4501-2, arXiv:1406.5375. [Addendum: Eur.Phys.J.C 76, 642 (2016)].

[4] CMS Collaboration, "Measurement of the $t\bar{t}$ production cross section in the $e\mu$ channel in proton-proton collisions at sqrt(s) = 7 and 8 TeV", *JHEP* **08** (2016) 029, doi:10.1007/JHEP08(2016)029, arXiv:1603.02303.

[5] CMS Collaboration, "Measurements of the $\mathrm{t\bar{t}}$ production cross section in lepton+jets final states in pp collisions at 8 TeV and ratio of 8 to 7 TeV cross sections", *Eur. Phys. J. C* **77** (2017) 15, doi:10.1140/epjc/s10052-016-4504-z, arXiv:1602.09024.

[6] ATLAS Collaboration, "Measurement of the $t\bar{t}$ production cross-section using $e\mu$ events with b-tagged jets in pp collisions at $\sqrt{s}$=13 TeV with the ATLAS detector", *Phys. Lett. B* **761** (2016) 136, doi:10.1016/j.physletb.2016.08.019, arXiv:1606.02699. [Erratum: Phys.Lett.B 772, 879–879 (2017)].

[7] CMS Collaboration, "Measurement of the top quark pair production cross section in proton-proton collisions at $\sqrt{s} = 13$ TeV", *Phys. Rev. Lett.* **116** (2016) 052002, doi:10.1103/PhysRevLett.116.052002, arXiv:1510.05302.

[8] CMS Collaboration, "Measurement of the $t\bar{t}$ production cross section using events in the eμ final state in pp collisions at $\sqrt{s} = 13$ TeV", *Eur. Phys. J. C* **77** (2017) 172, doi:10.1140/epjc/s10052-017-4718-8, arXiv:1611.04040.

[9] CMS Collaboration, "Measurement of the $t\bar{t}$ production cross section using events with one lepton and at least one jet in pp collisions at $\sqrt{s}$ = 13 TeV", *JHEP* **09** (2017) 051, doi:10.1007/JHEP09(2017)051, arXiv:1701.06228.

[10] LHCb Collaboration, "Measurement of forward top pair production in the dilepton channel in pp collisions at $\sqrt{s} = 13$ TeV", *JHEP* **08** (2018) 174, doi:10.1007/JHEP08(2018)174, arXiv:1803.05188.

[11] ATLAS, CMS Collaboration, "Combinations of single-top-quark production cross-section measurements and —$f_{LV}V_{tb}$— determinations at $\sqrt{s}$ = 7 and 8 TeV with the ATLAS and CMS experiments", *JHEP* **05** (2019) 088, doi:10.1007/JHEP05(2019)088, arXiv:1902.07158.

[12] ATLAS Collaboration, "Measurement of the inclusive cross-sections of single top-quark and top-antiquark t-channel production in pp collisions at $\sqrt{s}$ = 13 TeV with the ATLAS detector", *JHEP* **04** (2017) 086, doi:10.1007/JHEP04(2017)086, arXiv:1609.03920.

[13] CMS Collaboration, "Measurement of differential cross sections and charge ratios for t-channel single top quark production in proton–proton collisions at $\sqrt{s} = 13$ TeV", *Eur. Phys. J. C* **80** (2020) 370, doi:10.1140/epjc/s10052-020-7858-1, arXiv:1907.08330.

[14] ATLAS Collaboration, "Measurement of the cross-section for producing a W boson in association with a single top quark in pp collisions at $\sqrt{s} = 13$ TeV with ATLAS", *JHEP* **01** (2018) 063, doi:10.1007/JHEP01(2018)063, arXiv:1612.07231.

[15] J. de Favereau de Jeneret et al., "High energy photon interactions at the LHC", 2009. arXiv:0908.2020.

[16] D. d'Enterria and J.-P. Lansberg, "Study of Higgs boson production and its $b\bar{b}$ decay in $\gamma\gamma$ processes in proton-nucleus collisions at the LHC", *Phys. Rev. D* **81** (2010) 014004, doi:10.1103/PhysRevD.81.014004, arXiv:0909.3047.

[17] S. Fayazbakhsh, S. T. Monfared, and M. Mohammadi Najafabadi, "Top Quark Anomalous Electromagnetic Couplings in Photon-Photon Scattering at the LHC", *Phys. Rev. D* **92** (2015) 014006, doi:10.1103/PhysRevD.92.014006, arXiv:1504.06695.

[18] M. Łuszczak, L. Forthomme, W. Schäfer, and A. Szczurek, "Production of $t\bar{t}$ pairs via $\gamma\gamma$ fusion with photon transverse momenta and proton dissociation", *JHEP* **02** (2019) 100, doi:10.1007/JHEP02(2019)100, arXiv:1810.12432.

[19] V. P. Gonçalves, D. E. Martins, M. S. Rangel, and M. Tasevsky, "Top quark pair production in the exclusive processes at the LHC", *Phys. Rev. D* **102** (2020) 074014, doi:10.1103/PhysRevD.102.074014, arXiv:2007.04565.

[20] J. Howarth, "Elastic Potential: A proposal to discover elastic production of top quarks at the Large Hadron Collider", 2020. arXiv:2008.04249.

[21] CMS Collaboration, "The CMS Precision Proton Spectrometer at the HL-LHC – Expression of Interest", 2021. arXiv:2103.02752.

[22] CMS, TOTEM Collaboration, "CMS-TOTEM Precision Proton Spectrometer", Technical Report CERN-LHCC-2014-021, TOTEM-TDR-003, CMS-TDR-13, 9, 2014.

[23] G. Ruggiero et al., "Characteristics of edgeless silicon detectors for the Roman Pots of the TOTEM experiment at the LHC", *Nucl. Instrum. Meth. A* **604** (2009) 242, doi:10.1016/j.nima.2009.01.056.

[24] CMS, TOTEM Collaboration, "The CT-PPS tracking system with 3D pixel detectors", *JINST* **11** (2016) C11027, doi:10.1088/1748-0221/11/11/C11027.

[25] CMS Collaboration, "Particle-flow reconstruction and global event description with the CMS detector", *JINST* **12** (2017) P10003, doi:10.1088/1748-0221/12/10/P10003, arXiv:1706.04965.

[26] CMS Collaboration, "Performance of electron reconstruction and selection with the CMS detector in proton-proton collisions at $\sqrt{s} = 8$ TeV", *JINST* **10** (2015) P06005, doi:10.1088/1748-0221/10/06/P06005, arXiv:1502.02701.

[27] CMS Collaboration, "Performance of the CMS muon detector and muon reconstruction with proton-proton collisions at $\sqrt{s} = 13$ TeV", *JINST* **13** (2018) P06015, doi:10.1088/1748-0221/13/06/P06015, arXiv:1804.04528.

[28] M. Cacciari, G. P. Salam, and G. Soyez, "The anti-k_t jet clustering algorithm", *JHEP* **04** (2008) 063, doi:10.1088/1126-6708/2008/04/063, arXiv:0802.1189.

[29] M. Cacciari, G. P. Salam, and G. Soyez, "FastJet user manual", *Eur. Phys. J. C* **72** (2012) 1896, doi:10.1140/epjc/s10052-012-1896-2, arXiv:1111.6097.

[30] CMS Collaboration, "Jet energy scale and resolution in the CMS experiment in pp collisions at 8 TeV", *JINST* **12** (2017) P02014, doi:10.1088/1748-0221/12/02/P02014, arXiv:1607.03663.

[31] CMS Collaboration, "Performance of missing transverse momentum reconstruction in proton-proton collisions at $\sqrt{s} = 13$ TeV using the CMS detector", *JINST* **14** (2019) P07004, doi:10.1088/1748-0221/14/07/P07004, arXiv:1903.06078.

[32] CMS Collaboration, "Technical proposal for the Phase-II upgrade of the Compact Muon Solenoid", CMS Technical Proposal CERN-LHCC-2015-010, CMS-TDR-15-02, 2015.

[33] CMS, TOTEM Collaboration, "Proton reconstruction with the Precision Proton Spectrometer in Run 2", CMS Physics Analysis Summary CERN-TOTEM-NOTE-2022-001, CMS-PAS-PRO-21-001, Mar, 2022.

[34] GEANT4 Collaboration, "GEANT4: A simulation toolkit", *Nucl. Instrum. Meth. A* **506** (2003) 250, doi:10.1016/S0168-9002(03)01368-8.

[35] M. Boonekamp et al., "FPMC: A Generator for forward physics", 2011. arXiv:1102.2531.

[36] V. M. Budnev, I. F. Ginzburg, G. V. Meledin, and V. G. Serbo, "The Two photon particle production mechanism. Physical problems. Applications. Equivalent photon approximation", *Physics Reports* **15** (1975) 181, doi:10.1016/0370-1573(75)90009-5.

[37] P. Artoisenet, R. Frederix, O. Mattelaer, and R. Rietkerk, "Automatic spin-entangled decays of heavy resonances in Monte Carlo simulations", *JHEP* **03** (2013) 015, doi:10.1007/JHEP03(2013)015, arXiv:1212.3460.

[38] P. Nason, "A New method for combining NLO QCD with shower Monte Carlo algorithms", *JHEP* **11** (2004) 040, doi:10.1088/1126-6708/2004/11/040, arXiv:hep-ph/0409146.

[39] S. Frixione, P. Nason, and C. Oleari, "Matching NLO QCD computations with Parton Shower simulations: the POWHEG method", *JHEP* **11** (2007) 070, doi:10.1088/1126-6708/2007/11/070, arXiv:0709.2092.

[40] S. Alioli, P. Nason, C. Oleari, and E. Re, "A general framework for implementing NLO calculations in shower Monte Carlo programs: the POWHEG BOX", *JHEP* **06** (2010) 043, doi:10.1007/JHEP06(2010)043, arXiv:1002.2581.

[41] M. Czakon et al., "Top-pair production at the LHC through NNLO QCD and NLO EW", *JHEP* **10** (2017) 186, doi:10.1007/JHEP10(2017)186, arXiv:1705.04105.

[42] T. Sjöstrand, S. Mrenna, and P. Skands, "PYTHIA 6.4 physics and manual", *JHEP* **05** (2006) 026, doi:10.1088/1126-6708/2006/05/026, arXiv:hep-ph/0603175.

[43] T. Sjöstrand et al., "An introduction to PYTHIA 8.2", *Comput. Phys. Commun.* **191** (2015) 159, doi:10.1016/j.cpc.2015.01.024, arXiv:1410.3012.

[44] CMS Collaboration, "Extraction and validation of a new set of CMS PYTHIA8 tunes from underlying-event measurements", *Eur. Phys. J. C* **80** (2020) 4, doi:10.1140/epjc/s10052-019-7499-4, arXiv:1903.12179.

[45] NNPDF Collaboration, "Parton distributions from high-precision collider data", *Eur. Phys. J. C* **77** (2017) 663, doi:10.1140/epjc/s10052-017-5199-5, arXiv:1706.00428.

[46] CMS Collaboration, "Performance of the CMS Level-1 trigger in proton-proton collisions at $\sqrt{s} = 13$ TeV", *JINST* **15** (2020) P10017, doi:10.1088/1748-0221/15/10/P10017, arXiv:2006.10165.

[47] CMS Collaboration, "The CMS trigger system", *JINST* **12** (2017) P01020, doi:10.1088/1748-0221/12/01/P01020, arXiv:1609.02366.

[48] CMS Collaboration, "Identification of heavy-flavour jets with the CMS detector in pp collisions at 13 TeV", *JINST* **13** (2018) P05011, doi:10.1088/1748-0221/13/05/P05011, arXiv:1712.07158.

[49] CMS Collaboration, "Measurements of $\mathrm{t\bar{t}}$ differential cross sections in proton-proton collisions at $\sqrt{s} = 13$ TeV using events containing two leptons", *JHEP* **02** (2019) 149, doi:10.1007/JHEP02(2019)149, arXiv:1811.06625.

[50] L. Breiman, J. Friedman, R. A. Olshen, and C. J. Stone, "Classification and regression trees". Chapman and Hall/CRC, 1984. ISBN 978-0-412-04841-8.

[51] A. Hocker et al., "TMVA - Toolkit for Multivariate Data Analysis", 2007. arXiv:physics/0703039.

[52] J. H. Friedman, "Data Analysis Techniques for High-Energy Particle Physics", in *3rd CERN School of Computing*. 10, 1974.

[53] CMS Collaboration, "CMS luminosity measurement for the 2017 data-taking period at $\sqrt{s} = 13$ TeV", CMS Physics Analysis Summary CMS-PAS-LUM-17-004, CERN, Geneva, 2018.

[54] J. Butterworth et al., "PDF4LHC recommendations for LHC Run II", *J. Phys. G* **43** (2016) 023001, doi:10.1088/0954-3899/43/2/023001, arXiv:1510.03865.

[55] R. J. Barlow and C. Beeston, "Fitting using finite Monte Carlo samples", *Comput. Phys. Commun.* **77** (1993) 219, doi:10.1016/0010-4655(93)90005-W.

[56] G. Cowan, K. Cranmer, E. Gross, and O. Vitells, "Asymptotic formulae for likelihood-based tests of new physics", *Eur. Phys. J. C* **71** (2011) 1554, doi:10.1140/epjc/s10052-011-1554-0, arXiv:1007.1727. [Erratum: Eur.Phys.J.C 73, 2501 (2013)].